

# Persistence Length and Phases of a Flexible Polymers with Dipole Interactions

B.B. Rodrigues,<sup>1,\*</sup> J.C.S. Rocha,<sup>2,†</sup> and B.V. Costa<sup>1,‡</sup>

<sup>1</sup>*Laboratório de Simulação, Departamento de Física, ICEX*

*Universidade Federal de Minas Gerais, 31720-901 Belo Horizonte, Minas Gerais, Brazil*

<sup>2</sup>*Departamento de Física, ICEB, Universidade Federal de Ouro Preto, 34000-000 Ouro Preto, Minas Gerais, Brazil*

(Dated: July 19, 2022)

The thermodynamic and elastic properties of a flexible polymer in the presence of dipole interactions are studied via Monte Carlo simulations. The structural coil-globular, solid-globular, and solid-solid transitions are mapped in the hyperphase diagram, parameterized by the dipole concentration,  $\eta$ , and temperature,  $T$ . Polymer flexibility is usually quantified by the persistent length,  $\ell_p$ , which is defined as the length on which the bond-bond correlation is lost. Non-monotonic flexibility of polymeric complexes as a function of  $\eta$  has been interpreted as a cooperative effect under the Worm-Like Chain model. Instead of the usual exponential behavior,  $\langle C(k) \rangle \propto e^{-k/\ell_p}$ , here we show that the bond-bond correlation follows a power law decay,  $\langle C(k) \rangle \approx c_0 k^{-\omega}$ . The power law regime holds even at the coil-globular transition, where a Gaussian limit is expected, originated from non-leading terms due to monomer-monomer connectivity. The exponent  $\omega$  monotonically converges to the SAW limit for large  $\eta$ , if the isotherm pathway is constructed at the coil phase. The deviation from ideality is better probed at the chain segment size, and the expected  $\Theta$ -condition at the  $(T, \eta)$  pathway near the coil-globular transition is not observed.

PACS numbers: 05.70.Fh, 05.10.Ln 61.25.he

## I. INTRODUCTION

The understanding of mechanical properties of polymers like aggregation, cluster formation and flexibility are central issues in a number of areas, ranging from production of nano-structured materials [1] to the development of molecular-engineered pharmaceutical drugs [2]. Of particular interest is the introduction of electric dipole interactions among monomers in the polymer which affect its electrical and mechanical properties [3]. Electroactive polymers belong to the important category of smart materials with promising applications in several fields. In many cases the introduction of polar particles make so drastic modification that the stiffness of the polymer changes abruptly compressing the molecule by many orders of magnitude [4]. Several biological processes are mediated by such interactions, as when molecules irreversibly bind to DNA, forming DNA+molecule complexes [5–11]. In energy storage applications, it is possible to store more energy in dielectric composites because of additional polarization of the inclusions and interfaces [12]. Widely used to characterize the flexibility of a polymer is the so-called persistence length,  $\ell_p$ , [13, 14], usually measured by fitting a force *versus* extension curve at the entropic regime [15]. This concept was borrowed from the Worm-Like Chain (WLC) [16], or Kratky-Porod model, which is nothing but the correlation length measured along the polymer chain. If we consider a long polymer consisting of  $N$  monomers with

bond length  $\Delta \vec{r}_i = \vec{r}_{i+1} - \vec{r}_i$ , the correlation along the chain is given by

$$\langle C(k) \rangle \equiv \langle \cos \theta(k) \rangle = \frac{\langle \Delta \vec{r}_i \cdot \Delta \vec{r}_{i+k} \rangle}{\langle \Delta \vec{r}_i^2 \rangle}, \quad (1)$$

where  $\langle \dots \rangle$  represents average over thermal fluctuations. For linear chains following Gaussian statistics, the correlation  $\langle C(k) \rangle$  is expected to decay exponentially with the distance as

$$\langle C(k) \rangle \propto e^{-k\ell/\ell_p} \quad . \quad (2)$$

Here  $\ell = \sqrt{\langle \vec{r}_i^2 \rangle}$  and  $\ell_p$  measures the polymer flexibility. Results from force *versus* extension experiments on polymers (DNA) with ligands [8, 9] have shown a non monotonic behavior for  $\ell_p$  as a function of ligand concentration,  $\eta$ , which can not be understood by the usual WLC model. More recently the behavior was explained as a cooperative effect introduced by the ligands, which locally change the chain flexibility,  $\ell_p^i$  [17]. They supposed ligand molecules irreversibly bind to DNA according to a Hill-type equation and follow the quenched disordered statistics. The model relies on the assumption that bond-bond correlations decay exponentially, and the effective flexibility,  $\ell_p^{eff}$ , obeys the WLC model. However, an exponential decay only holds when the chain follows a Gaussian statistics, at any other condition the correlation function decays as a power law

$$\langle C(k) \rangle \propto k^{-\omega} \quad . \quad (3)$$

For dilute polymers in good solvent conditions,  $\omega = 2(1 - \nu)$ , where  $\nu$  is the Flory exponent characteristic of the chain size. At the Self-Avoiding Walk (SAW) limit,  $\nu = 0.588$ , leading to  $\omega = 0.824$  [18]. The exponential

\*Electronic mail: bbr@fisica.ufmg.br

†Electronic mail: jcsrocha@ufop.edu.br

‡Electronic mail: bvc@fisica.ufmg.br

decay has also been ruled out for polymer melts (Flory's ideality hypothesis [19]) both theoretically and numerically [20–22], due to a coupling of static fluctuations of adjacent subchains, and a power-law exponent  $\omega = 3/2$  is observed. Interestingly, the same result was found in single-chain polymers due to a non-uniform probability of the distance between two monomers as a function of the distance along the chain [23]. The result was derived for a two-body model with bead-spring interactions and corroborated by computer simulations of the same bead-spring model with off-chain LJ interactions. More recently, H-P. Hsu et al [24] discussed the conditions under which the WLC model holds “and the question to what extent the persistence length depends on external conditions (such as solvent quality) is considered”. Two independent groups reported that the unusual behavior of single-stranded DNA (ssDNA) force *versus* extension experiments [25] could be explained if the bond-bond correlations of a polyelectrolyte chain obey a power-law decay, in agreement with Eq. 3. The exponent  $\omega$  was also determined by Toan et al [26], and Mark et al [27] obtaining a value between 0.2 and 0.7 and  $\omega = 0.55$  respectively.

The polymer chain size is a power-law function of the number of monomers  $N$  [13, 14]. Extending this concept to a segment chain size (as a function of  $k$ ) we have

$$R_c^2(k) = a_0 k^{2\nu}, \quad (4)$$

where  $\nu$  is the universal exponent, and  $a_0$  is non-universal, although the ratio between two measurements of a chain size (such as end-to-end distance and radius of gyration) is indeed universal. The generalized segment chain size is defined as

$$\langle R_c^2(j-i) \rangle = \langle |\vec{r}_j - \vec{r}_i|^2 \rangle, \quad (5)$$

where  $j = i + k$  and averages are taken over all pairs of  $(i, j)$  for a given  $k$ . The right hand side (r.h.s.) of Eq. 1 can be written as

$$\begin{aligned} \langle \Delta \vec{r}_i \cdot \Delta \vec{r}_j \rangle &= \langle \partial_i \vec{r}_i \cdot \partial_i \vec{r}_j \rangle \\ &= -\frac{1}{2} \partial_i \partial_j \langle R_c^2(j-i) \rangle, \end{aligned} \quad (6)$$

which leads to

$$\langle C(k) \rangle = \frac{c_1}{\langle \Delta \vec{r}_i^2 \rangle} k^{-2(1-\nu)}, \quad (7)$$

where  $c_1 = \nu(2\nu - 1)$ . The values for  $\nu$  in a non-collapsed chain are known for Gaussian (ideal), Rod-like and SAW phases [18]. Considering the closure relation between  $\omega$  and  $\nu$ , the following values for  $\omega$  are derived

$$\nu = \begin{cases} 1/2 & \rightarrow \omega = 1 \quad \text{Gaussian}, \\ 0.588 & \rightarrow \omega = 0.824 \quad \text{SAW}, \\ 1 & \rightarrow \omega = 0 \quad \text{Rod-like}. \end{cases}$$

In this framework, the limit  $\nu \rightarrow 1/2$  leads to  $c_1 \rightarrow 0$ , and the bond-bond correlations decay exponentially. Considering that connectivity introduces a correction to the

squared chain size proportional to the mean squared segment distance along the chain ( $k$ ), we have

$$R_c^2(k) = a_0 k^{2\nu} \left( 1 - b_0 k^{-1/2} \right). \quad (8)$$

Therefore, bond-bond correlations near the  $\Theta$ -point are

$$\langle C(k) \rangle = \frac{c_2}{\langle \Delta \vec{r}_i^2 \rangle} k^{-3/2}, \quad (9)$$

where  $\nu = 1/2$  is assumed. Note that the coefficient  $c_2$  does not vanish in this derivation. The closure condition in this case is  $\omega = d\nu$  with  $d = 3$ .

The goal in this work is to use Monte Carlo simulations to study the morphology and mechanical properties of a polymer where ligands are introduced in the chain. We applied the Wang-Landau algorithm to study the phase diagram and the more representative morphology at each structural phase of the system and the Metropolis algorithm to obtain the correlation function near the extended phase. A complete characterization of both the segment chain sizes and the correlations as a function of both temperature and ligand concentration paves the condition under which the correction term becomes dominant, due to chain connectivity. The polymer flexibility is intimately related to its morphology. We can argue if the addition of ligands will change the phases in the system. In face of its technological importance and theoretical challenge, it is important to understand the polymer behavior upon introduction of polar particles. As a main result, we show how the correlations decay obeys a power-law even when the polymer approaches the CG transition in a hyperphase diagram of varying temperature and ligand concentration in a quenched-disordered polymer. So, when both monomer-monomer and monomer-solvent interactions are considered, the  $\Theta$ -point condition (mapped into a line at the  $(T, \eta)$  plane) does not lead to exponential decay of the correlations.

The Wang-Landau (WL) [28] technique has proven to successfully sample both thermal and structural polymer properties [29–32] unraveling details of different structural phases even in the more unamenable situations. However, it becomes very difficult to sample the correlation functions,  $C(k)$ , using this approach. To obtain  $C(k)$  we implemented the Metropolis algorithm. This allowed us to access larger systems than in the former case. The paper is organized as follows. In Sec. II, we describe the polymer model we used. Both WL and Metropolis (And Simulated Annealing) techniques are briefly addressed in Sec. III, followed by a description of how we calculate thermal and quenched disorder averages. In Sec. IV we present our results for the hyperphase diagram, where structural coil-globular, (CG), solid-globular, (SG), and solid-solid, (SS), transitions are shown. We also analyze the bond-bond correlations as well as the segment chain size near the CG transition. Finally, in Sec. V we summarize our findings and suggest further investigations that have not been addressed in this study.

## II. MODEL

To our computational experiment we chose an atomistic point of view to model the polymer. As usual the monomers are considered as spherical beads interacting with each other through the extensively used Lennard-Jones (6-12) potential and the anharmonic FENE (Finitely Extensible Nonlinear Elastic) potentials.

$$V_{\text{LJ}}(r_{ij}) = 4\epsilon \left[ \left( \frac{\sigma}{r_{ij}} \right)^{12} - \left( \frac{\sigma}{r_{ij}} \right)^6 \right] - V_{\text{LJ}}(r_1) \quad , \quad (10)$$

and

$$V_{\text{F}}(r_{i,i+1}) = -\frac{1}{2}k_0R^2 \ln \left[ 1 - \left( \frac{r_{i,i+1} - r_0}{R} \right)^2 \right] \quad , \quad (11)$$

where  $r_{ij}$  is the distance between monomers at positions  $i$  and  $j$ ,  $\sigma = 2^{-1/6}r_0$  is the effective radius of the monomer in units of  $r_0$ , which is the minimum of the LJ potential and sets the reduced length unit. A cutoff at  $r_1 = 5\sigma$  is introduced, and  $V_{\text{LJ}}$  is shifted  $V_{\text{LJ}}(r_1) \approx -10^{-6}$ . For  $r_{ij} > r_1$ ,  $V_{\text{LJ}}(r_{ij}) = 0$ . The potential depth  $\epsilon$  is set to unity and energy is given in dimensionless units  $E/\epsilon$ . In  $V_{\text{F}}$  we set, as usual, the stiffness constant  $k_0 = 40$  and the finite extensibility  $R = 3/7$ . Particles with a dipole charge, from now on named ligands for simplicity, can randomly attach to the polymer chain in an irreversible way. We assume that ligand+monomer sites have one unit charge, which gives rise to Coulomb repulsion screened by the implicit solvent. The resulting coarse-grained procedure is represented in Fig. 1. Yellow spheres represent monomer bare site, whereas green spheres are for the monomers with ligand particles attached. The total energy of this system is given by

$$\mathcal{H} = \sum_{i=1}^{N-1} V_{\text{F}}(r_{i,i+1}) + \sum_{i=1}^{N-1} \sum_{j=i+1}^N [V_{\text{LJ}}(r_{ij}) + V_{\text{YK}}(r_{ij})] . \quad (12)$$

where  $V_{\text{YK}}$  is the screened repulsion Coulomb energy,

$$V_{\text{YK}}(r_{ij}) = \frac{\alpha^2}{r_{ij}} e^{-r_{ij}/\xi} - V_{\text{YK}}(r_2) \quad , \quad (13)$$

where  $\alpha^2$  controls the magnitude of the repulsion and  $\xi$  is the effective shielding length. We set  $\alpha^2 = 0.4$  and  $\xi = 1.0$ . As usual, a cutoff,  $r_2 = 8\sigma$ , is introduced in order to speedup the calculations. To determine the phase diagram of the model we implemented the Replica-Exchange Wang-Landau (REWL) [33] algorithm simulating systems with  $N = 20, 50$  and  $70$  monomers and ligand concentration  $\eta = 0, 10, 20, \dots, 100\%$ . The correlation function is obtained by using a Metropolis scheme as detailed below.

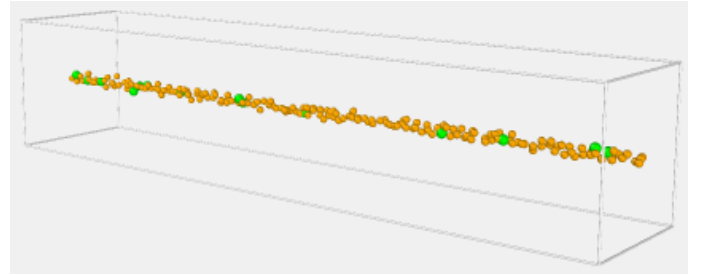


FIG. 1: (Color online) *Left:* Atomistic representation of a polymer with ligands. Each bare monomer site is replaced as a yellow sphere, whereas a site with ligand is replaced by a green sphere.

## III. SIMULATION DETAILS

The WL method provides an estimate for the Density of State (DOS) by sampling numerous configurations in the entire considered energy spectrum. In order to efficiently sample all the configuration space we propose the following trial moves for the monomers on the chain: Energy-dependent random displacement, crank-shaft and pivotatation [34]. Those proposed configurations are accepted with the probability  $P_{i \rightarrow f} = \min \left\{ \frac{g(E_i)}{g(E_f)}, 1 \right\}$ , where  $g(E)$  is the iteratively estimated DOS within the energy interval  $E$  and  $E + \delta E$ . One Monte Carlo sweep (MCS) consists of  $N$  single monomer random displacement and one of each of the other types of trial moves. The minimum modification factor is set to  $\ln f = 10^{-8}$  with flatness criterion  $p = 0.7$ . Energy bin width is set to  $\delta E = 0.05$ .  $E_{\text{max}} = 3.0N$  and  $E_{\text{min}}$  are calculated iteratively, which leads to  $n_{\text{bin}} \propto 10^4$  energy bins. Statistics for thermal and structural quantities are collected after  $g(E)$  stabilizes, provided that each energy bin is visited at least  $10^7$  times. With this detailed procedure, the logarithm of the density of states,  $\ln [g(E)]$ , is evaluated in a range involving a thousand orders of magnitude between the maximum and minimum values. The following structural quantities are calculated: the radius of gyration

$$R_g^2 = \frac{1}{N} \sum_{i=1}^N (\vec{r}_i - \vec{r}_{\text{CM}})^2 , \quad (14)$$

where  $\vec{r}_{\text{CM}}$  are the coordinates of the center of mass of the polymer, the squared end-to-end distance

$$R_{\text{ee}}^2 = (\vec{r}_N - \vec{r}_1)^2 , \quad (15)$$

and the contour length

$$R_c = \sqrt{R_{\text{ee}}^2} . \quad (16)$$

Initial configurations with quenched ligands are independently created as follows. For a chain with  $N$  monomers and ligand concentration  $\eta(\%)$ , we randomly distribute  $N_\ell = \eta \times N$  ligands along the chain. Hence, the probability of each configuration  $X = \{x_i\}$  to be generated is

$P[X] = 1/\binom{N}{N_\ell}$ , where  $X$  is a set of  $N$  values,  $x_i = 1$  if the  $i^{\text{th}}$  monomer has a ligand and  $x_i = 0$  otherwise, which uniquely describes the ligand occupation along the polymer chain. The YK interaction in Eq. 12 is then evaluated only between monomers labelled with  $x_i = 1$ . Understandably each initial configuration leads to a distinct DOS. We use brackets,  $\langle \dots \rangle$ , to denote thermal averages while a bar,  $\overline{\dots}$ , is used for averages over the quenched disorder. The partition function for each DOS is

$$Z[X]_T = \sum_{E[X]} g(E[X]) e^{-\beta E[X]}, \quad (17)$$

where  $\beta \equiv 1/k_B T$  is the inverse temperature (We will take  $k_B = 1$  from now on). Canonical structural quantities for each initial configuration are calculated as

$$\langle A[X] \rangle_T = \frac{\sum_{E[X]} A(E[X]) g(E[X]) e^{-\beta E[X]}}{Z[X]_T}, \quad (18)$$

and the average over the disorder is

$$\overline{\langle A[X] \rangle}_T = \sum_X P[X] \langle A[X] \rangle_T. \quad (19)$$

The free energy,  $F(T)$ , is calculated as [35]

$$\begin{aligned} F(T) &= -\beta^{-1} \overline{\ln Z[X]_T}, \\ &= -\beta^{-1} \sum_X P[X] \ln Z[X]_T. \end{aligned} \quad (20)$$

Thermal quantities are calculated as derivatives of Eq. 20. The ligands introduce the so-called pairwise disorder, which is translationally invariant. Error bars in our calculations are obtained by averaging over different many initial distributions. For the sake of clarity, we utilize only the brackets notation,  $\langle \dots \rangle$ , for both thermal and quenched averages along the rest of the paper.

Metropolis with Simulated Annealing algorithm [36] is more adequate for sampling bond-bond correlations,  $\langle C(k) \rangle$ , where long polymer chains at specific temperatures can be addressed with more statistics. The MC moves are the same as defined for WL algorithm. Simulation starts at  $T = 10.0$  and, for each temperature,  $n_{\text{eq}} = 10^6 N$  moves are set for equilibration. After equilibration we average  $\langle C(k) \rangle$  over  $n_{\text{sim}} = 20 \times n_{\text{eq}}$  samples. Annealing temperature steps are set to  $\Delta T = 0.5$  for  $T \in [10.0, 5.0]$  and  $\Delta T = 0.1$  for  $T \in [5.0, 1.0]$ .  $\langle C(k) \rangle$  is measured for polymer chains of  $N = 20, 50, 70, 100, 200$  and 1,000 monomers. The final intrachain quantities (which comprise bond-bond correlations, intrachain end-to-end and radius of gyration measurements) are the result of both thermal and quenched averages over at least 100 independent runs with random ligand distributions  $X$  for each  $\eta$ . To collect statistics in the vicinity of the coil-globular transition,  $T \approx T_{\text{CG}}$ , a setup of 100 independent simulations is performed with different cooling rates ( $\Delta T = 1.0, 0.5$  and  $0.1$ ), starting at  $T = 10.0$  to ensure a better sampling.

## IV. RESULTS AND DISCUSSION

### A. Thermal Fluctuations

We first analyze the structural quantities as a function of temperature and ligand concentration from REWL. In Fig. 2 (a),  $\langle R_{\text{ee}}^2(T) \rangle$  as a function of temperature is shown for  $N = 70$  monomers and  $\eta = 0, \dots, 100\%$ . In the globular phase (low  $T$ ) the end-to-end distance (averaged by the number of monomers) is expected to be small, and monotonically grows with temperature until reaching the extended phase (high  $T$ ). Our results show that the concentration of ligands not only increases the end-to-end distance in the extended phase but also reduces the temperature at which we observe its decay to near zero, i.e. it lowers the collapse temperature.

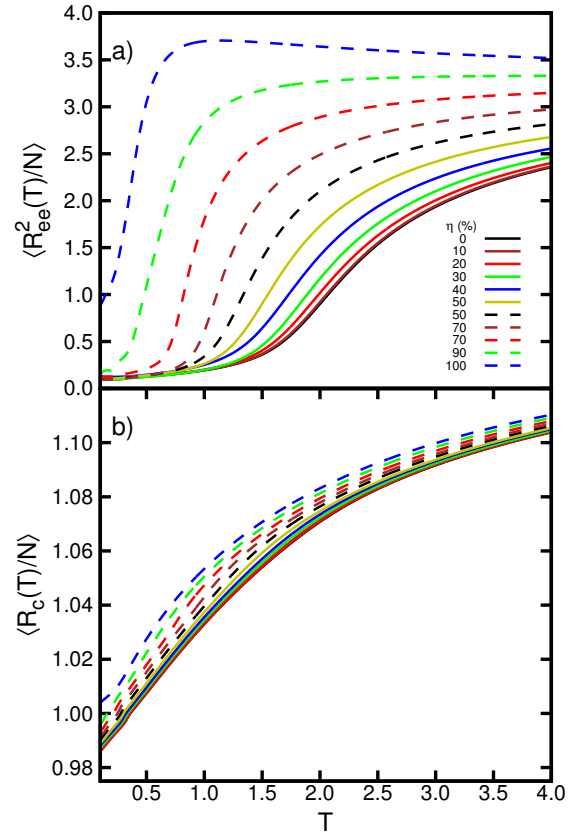


FIG. 2: (Color online) Squared end-to-end distance (a) and contour length (b) per monomer as a function of temperature for  $N = 70$  and  $\eta = 0, \dots, 100\%$ .

A similar behavior is observed for  $\langle R_g^2(T) \rangle$  (not shown here). In Fig. 2 (b),  $\langle R_c(T)/N \rangle$  is shown as a function of  $T$ , the symbols are the same as in (a). Although the contour length (per monomer unity) continuously increases with  $T$ , it does not show any clear distinction between the extended and collapsed phase and it is also not strongly

affected by increasing the ligand concentration, which is consistent with experiment results Ref. [17].

Fluctuations of thermodynamical and structural quantities are obtained as

$$d\langle A \rangle / dT = \frac{\langle EA \rangle - \langle E \rangle \langle A \rangle}{NT^2}. \quad (21)$$

Those fluctuations are used to locate the structural transitions on the canonical ensemble. The specific heat,  $\langle C_V \rangle = d\langle E \rangle / dT$  (black),  $d\langle R_g^2 \rangle / dT$  (red) and  $d\langle R_c \rangle / dT$  (blue) are shown in Fig. 3 for selected values of the ligand concentration. The quantity  $d\langle R_c \rangle / dT$  (blue) is shifted down by 2 units for clarity. Peaks on  $d\langle R_g^2 \rangle / dT$  at high  $T$  are the signature of a CG transition [37], and are indicated by a vertical red dashed line.

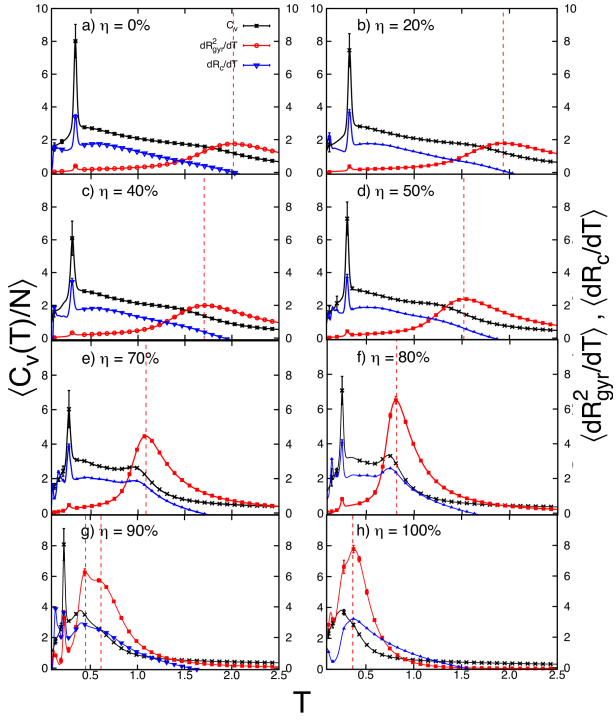


FIG. 3: (Color online) Specific heat  $\langle C_V \rangle$  (black) and thermal fluctuations of structural quantities  $d\langle R_g^2 \rangle / dT$  (red) and  $d\langle R_c \rangle / dT$  (blue) as a function of temperature for  $N = 70$  monomers. The latter quantity is shifted down by 2 units for clarity. From top left to bottom right:  $\eta (\%) = (a) 0, (b) 20, (c) 40, (d) 50, (e) - (h) 70 - 100$ . The red dashed lines indicate the CG transition temperature for each  $\eta$ . Error bars are smaller than the symbols, when not shown.

From panels (a) to (h) we observe that the *CG* transition temperature,  $T_{CG}$ , monotonically decreases with  $\eta$ . The chain collapse is prevented by the suppression of the entropic freedom brought in by the presence of ligands. Therefore, any configurational change is energetically costly, which is a characteristic of a good solvent where strong excluded volume (EV) interactions are dominant. A similar decrease on  $T_{CG}$  is found when a flexible polymer is subjected to bending restraints [29],

which also leads to high energetic penalty. The increase in thermal activity is signaled by  $\langle C_V \rangle$  curves at high  $T$ , where a “shoulder” continuously evolves to a peak by increasing  $\eta$ . For  $\eta = 90\%$ , two peaks can be identified in  $d\langle R_g^2 \rangle / dT$ , see Fig. 3 (g). The corresponding  $\langle C_V \rangle$  curve also shows thermal activity, signaled by a small peak followed by the “shoulder” development. The double peaks are actually the result of a two-step collapse, as will be discussed in the next section. A pronounced peak in  $\langle C_V \rangle$  at low  $T$  marks the SG transition [38, 39], observed in Fig. 3 from  $\eta = 0\%$  to  $90\%$ . For  $\eta = 100\%$ , the CG collapse is suppressed as the globular phase is no longer stable (see Section IV B). We observed that the corresponding solid phase is not a perfect crystal, but rather a composition of glassy meta-stable structures. In the solid phase, entropic degrees of freedom are highly suppressed, being the fluctuations dominated by the reorganization of surface monomer contacts and steric constraints [40, 41]. This reorganization also leads to thermal fluctuations of the contour length, signaled as a peak at  $d\langle R_c \rangle / dT$  (blue curve). Energetic penalty at the collapsed phase is mainly due to attractive reorganizations, therefore ligand-ligand repulsion have little influence. As a result, both position and height of  $\langle C_V \rangle$  and  $d\langle R_c \rangle / dT$  peaks are surprisingly similar for  $\eta < 100\%$ . A solid-solid transition is identified by the small peaks in  $d\langle R_c \rangle / dT$  at very low  $T$ . These signals arise from further accommodation of surface contacts of the solid structures. A more detailed investigation of these transitions requires sophisticated low-energy topological MC moves [40]. The quenched disordered statistics, however, forbids any topological change of the chain sequence. Both SS and SG transitions, although accurately mapped, are far below the temperatures at which the bond-bond correlations are measured in this study.

## B. Hyperphase diagram

The hyperphase diagram, depicted in Fig. 4, is constructed observing the structure of the quantities in Fig. 3. Each curve represents the boundary of structural transitions in Fig. 4 (a) as follows: Red squares are for CG, black dots are for SG and the SS transition is represented by blue triangles. The lines are only guide to the eyes. Representative equilibrium configurations for each structural phase are shown in Fig. 4 (b). Four different regions are identified in the  $(T, \eta)$  plane. The coil ( $C, C^*$ ) phase occurs at high temperature for all  $\eta$  values. It is a random vapour-like and structureless extended phase, dominated by EV interactions. While at low  $\eta$  the polymer is entropically driven and configurations  $C$  are unstructured, at high ligand concentration, ( $C^*$  configurations) local agglomerates are formed. These “blobs” change locally the chain flexibility. By lowering the temperature, the polymer undergoes a transition at  $T_{CG}$ , which decreases when  $\eta$  increases. The globular phase ( $G, G^*$ ) is characterized by the collapse of the polymer chain. When the ligand concentration increases, the polymer tends to trap

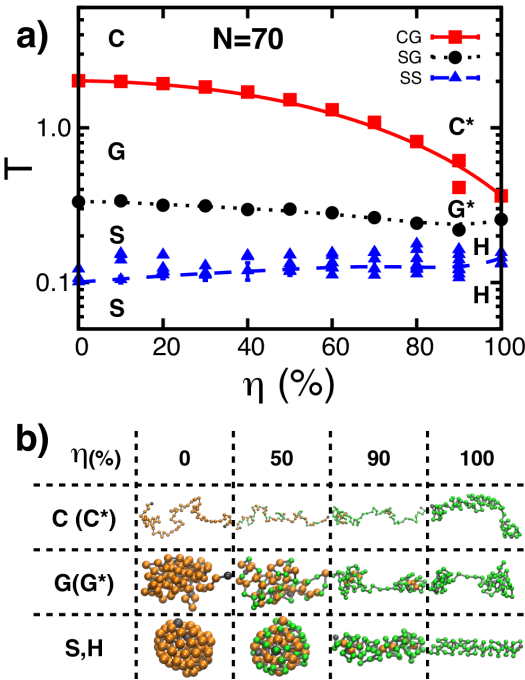


FIG. 4: (Color online). Hyperphase diagram for  $N = 70$  monomers. (a) Top figure shows the hyperphase diagram at the  $T, \eta$  plane. Lines are guide to the eyes. Error bars are smaller than the symbols when not visible. The region labeled  $C, C^*$  is a coil phase, although at higher  $\eta$  the polymer starts forming agglomerates. The region  $G$  corresponds to a globular phase. For  $\eta > 80\%$ , a two-globule structure  $G^*$  is observed (See the figure in the bottom). At very low  $T$ , the solid globular,  $S$  phase, is the equilibrium configuration for  $\eta < 90\%$ . Above this concentration, a zig-zag structure resembling a helix,  $H$ , appears. (b) Representative configurations for each structural phase mapped. Yellow spheres are for bare monomers and the green ones for monomers with ligands.

the bare monomers (yellow spheres) by surrounding them with ligand monomers (green spheres), eventually preventing the chain to collapse into a single globule, clearly seen in Fig. 4 (b) for  $\eta = 90\%$ . These structures are not found in similar on-lattice polyelectrolytes [42], which predicts a chain collapse into a single compact globule under cooling. The formation of two-droplets at  $\eta = 90\%$  is consistent with the two peaks observed at  $d\langle R_g^2 \rangle/dT$  on Fig. 3 (g). For  $\eta = 100\%$  the two-droplets configuration at the liquid phase is not stable, due to the strong intra-chain repulsion. This phase is characterized by partial collapses of chain segments, until the polymer freezes into a well-organized zigzagged structure at  $T_{SG}$ . The solid phase, ( $S, H$ ), has two different representative structures. For  $\eta < 90\%$ , the coil-globular liquid structure freezes into a solid-globular formed by spherical layers. As for  $N = 70$ , we are far from the “magic numbers” (the closest ones being 55 and 147), where full icosahedron layers are formed [37], and due to the quenched disorder, no crystalline structure is expected. For  $\eta \geq 90\%$ , the

solid-globular freezing is prevented due to strong steric repulsion. The more energetically favorable structure resembles a rodlike, but with twisted fibers, instead of linear. The twist is a natural way to minimize both the ligand-ligand repulsion and the monomer-monomer attraction. This structural transition has a high thermal activity, identified by the peak at  $\langle C_V \rangle$  on Fig. 3 (h). The stable zigzagged structure, observed for  $\eta = 100\%$ , may shed some light on the electrostatically-driven helical unwind of proteins [43]. Interestingly, the solid  $S$  phase has intense thermal activity, as seen by the numerous blue triangles at  $\eta = 80, 90$  and  $100\%$ . Transition temperatures for the bare polymer  $T_{CG}(\eta = 0) = 2.00(1)$  and  $T_{SG}(\eta = 0) = 0.33(1)$  are in excellent agreement with those predicted by scaling-laws from Ref. [37] where they found  $T_{CG} = 1.977(4)$  and  $T_{SG} = 0.33(1)$  for  $N = 70$ . The dashed (blue) line shows the solid-solid, SS, transition. We find  $T_{SS}(\eta = 0\%) = 0.1008(1)$ , follows a straight line in the entire range of ligand concentration. For a fully charged polymer,  $T_{SS}(\eta = 100\%) = 0.144(8)$ .

### C. Classification of structural transitions

The classification of structural transitions in finite systems is not a simple task, as traditional techniques require that the ratio between surface and volume entropy contributions tend to zero. Therefore, more sophisticated methods as for instance, Fisher zeros [44], Energy Probability Distribution zeros [45] or microcanonic analysis are meant to overcome this limitation. As both methods deal with the derivative of the microcanonical entropy, instead of the free energy, they are less sensitive to the finiteness of the system. The microcanonical properties are derived from the probability distribution  $P(E, T)$  at the transition temperature [46]. First-order transitions reveal a bimodal probability distribution, where each peak represents the energy of maximum probability for each phase above and below the transition, let us say  $B$  and  $A$ , respectively. The position of each peak gives the equilibrium energy of the respective phase (for a fixed temperature  $T$ ),  $E_A$  for the phase  $A$  and  $E_B$  for the phase  $B$ . In a first order transition, the system has an equal probability to be found in each phase, then the phases coexists. The distance in energy between the peaks,  $\Delta Q = |E_B - E_A|$ , is the latent heat. The bimodal form is directly connected with the microcanonical analysis for a first order transition [47], as discussed in the following.

The microcanonical entropy is defined as

$$S(E) \equiv k_B \ln [g(E)] \quad , \quad (22)$$

while the canonical free energy being

$$F(T) \equiv -k_B T \ln [Z(T)] \quad , \quad (23)$$

where  $Z(T)$  is the canonical partition function. Any equilibrium property can be obtained as derivatives of these two functions. The microcanonical inverse temperature is defined as

$$\beta_{mc} \equiv \beta(E) := \frac{dS(E)}{dE} . \quad (24)$$

A subscript is included to differentiate from the canonical temperature, defined as

$$\beta_{can} \equiv \beta(T) := \frac{1}{k_B T} . \quad (25)$$

With both equations 23 and 25, the average of any quantity,  $A(E)$ , in the canonical ensemble can be calculated as

$$\begin{aligned} \langle A(T) \rangle &= \sum_E A(E) e^{\ln g(E) - \beta_{can}[E - F(T)]} \\ &= \sum_E A(E) P(E, T) \end{aligned} \quad (26)$$

$P(E, T)$  is the canonical probability distribution. For a given temperature, the energy that maximizes the probability is defined as the equilibrium energy. Important quantities are obtained as derivatives of the logarithm of  $\ln P(E, T)$

$$-\ln P(E, T) = \ln g(E) - \beta_{can}[E - F(T)] . \quad (27)$$

with the first derivative with respect to the energy being

$$\frac{d}{dE} [-\ln P(E, T)] = \beta_{can}(T) - \beta_{mc}(E) , \quad (28)$$

and the corresponding second derivative

$$\frac{d^2}{dE^2} [-\ln P(E, T)] = -\gamma_{mc}(E) , \quad (29)$$

where  $\gamma_{mc}$  is the fugacity. In a first-order transition, the probability distribution has three critical points where its first derivative is zero (Two maxima and a minimum in between)

$$\frac{d}{dE} [-\ln P(E, T)] = 0 . \quad (30)$$

The solution of the equation above is

$$\beta_{mc}^{tr}(E_1) = \beta_{mc}^{tr}(E_2) = \beta_{mc}^{tr}(E_3) = \beta_{can}(T^{tr}) , \quad (31)$$

with the following conditions for the second derivatives

$$\begin{aligned} \gamma_{mc}^{tr}(E_1) &< 0, & \text{maximum} \\ \gamma_{mc}^{tr}(E_2) &> 0, & \text{minimum} \\ \gamma_{mc}^{tr}(E_3) &< 0, & \text{maximum.} \end{aligned} \quad (32)$$

These solutions require a positive value for the fugacity at some point between the two negative values. This point also represents the energy,  $E$ , at which the probability

distribution has its lowest value between the two phases  $A$  and  $B$ . In a canonical simulation, sampling around this region is strongly suppressed, due to the difference between the minimum and the peak probabilities posing as a thermodynamic barrier. We observe that this condition is the same as the first order microcanonical condition defined in Ref. [47].

In Fig. 5 we show the analysis of the structural transitions between solid and globular phases in the range  $\eta = 0, \dots, 90\%$  (panels  $a - j$ ). Those are clearly first order. The transition temperature is identified as a vertical blue line at the peak position. Also, it is presented the canonical energy,  $\langle E(T) \rangle$  as a red dashed line (the scale is read at the right vertical axis). The change in the energy,  $\langle E(T) \rangle = -\frac{\partial \log Z}{\partial \beta}$ , curvature occurs at the transition temperature. The lower panels describe the probability  $P(E, T)$  at  $T = T^{tr}$ , where the bimodal distribution is observed. The left peak (lower energy) is related to the equilibrium energy of the solid phase and is identified by a dashed vertical blue line, while the right peak locates the respective globular phase (higher energy) and its position is marked with a vertical dotted red line. The depth of the valley between both phases is proportional to the free energy barrier required for the transition to happen [48]. Within this framework, we can draw some interesting conclusions. First, an increase in the ligand concentration ( $\eta$ ) results in a decrease in the depth of the valley, up to  $\eta = 80\%$ . This means that within this range, an increase in the ligand concentration hinders the formation of the spherical solid phase, making this transition unstable at higher concentrations. For  $\eta = 90\%$ , the depth of the valley is even more pronounced than the one at zero concentration. However, we can see that the transition happens between a solid toroidal and a liquid globular phase (figure 4). This transition is, therefore, of first order, as we can see at the lower panel in figure 5  $j$ ). This result shows how a zig-zag very stable configuration naturally emerges from simple two-body potentials, in comparison with previous models where three-body (bending angles) and four-body (dihedral angles) potentials are required [30].

In its turn, continuous transitions are connected to peaks on the second order derivative of the free energy, hence, it is connected to higher order derivatives of the probability distribution. Indeed, an interpretation of the microcanonical analysis can be made as follows. A continuous transition lacks a phase coexistence, the probability function does not display a bimodal distribution. Likewise, no discontinuity is observed in the canonical energy as no latent heat is involved. Moreover, for finite systems, it is reasonable to argue that a range of temperature characterizes the transition. Therefore, a wide probability distribution for temperatures close to transition  $T^{tr}$  is expected. On the other hand, for  $T_A < T^{tr}$ , i.e. for the lower energy phase  $A$ , and for  $T_B > T^{tr}$ , i.e. for the higher energy phase  $B$ , the probability distribution is supposed to be narrower, leading to a higher peak in comparison with the transition temperature (considering

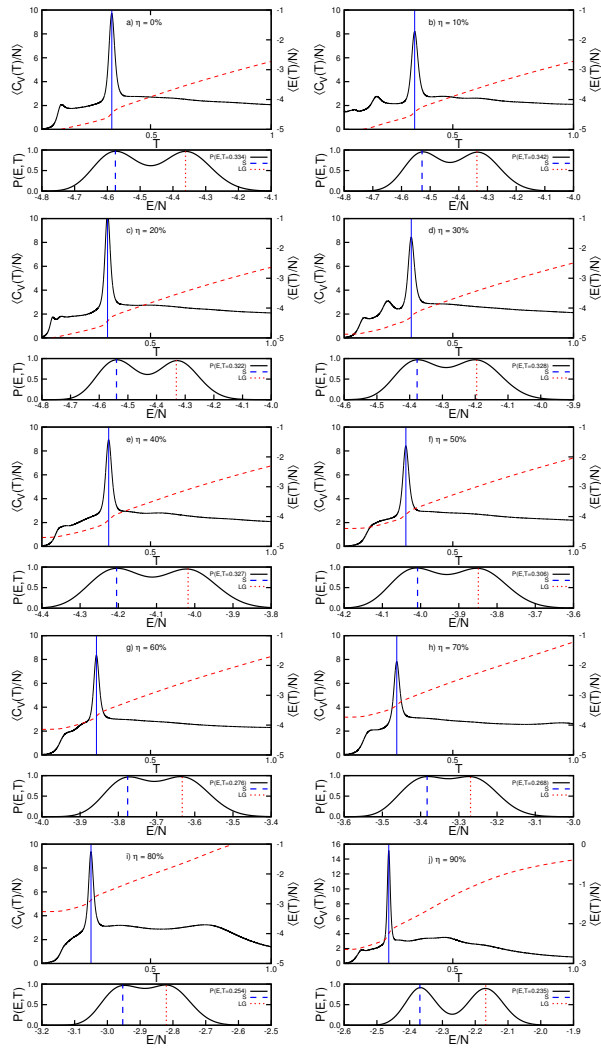


FIG. 5: (Color online) The figures show plots of the specific heat (black) and energy (red) as a function of temperature for  $\eta = 0, 10, \dots, 80$  and 90%. The vertical blue line marks the transition temperature. Just below each figure is also shown the respective plot for the probability  $P(E, T)$ . The first (blue) and second (red) peaks are for the equilibria temperature for solid and liquid globular phases, respectively. The change in the energy,  $\langle E(T) \rangle = -\frac{\partial \log Z}{\partial \beta}$ , curvature occurs at the transition temperature.

the total probability is  $\int_E P(E, T) = 1$ . The maximum of  $P(E, T)$  as a function of the temperature is defined as

$$F^{\text{MAX}}(E, T) = \max[-\ln P(E, T)]. \quad (33)$$

This condition was already defined as  $\beta_{\text{mc}}^{\text{tr}}(E) = \beta_{\text{can}}^{\text{tr}}(T)$  and  $\gamma_{\text{mc}}^{\text{tr}} < 0$ . However, in this case we collect only one point for each temperature. Introducing this condition at equation 33 leads to

$$F^{\text{MAX}}(E, T) = \ln g(E) - \frac{d \ln g(E)}{dE} [E - F(T)] \quad (34)$$

and the location of the maximum for a given temperature is obtained by the partial derivative with respect to the

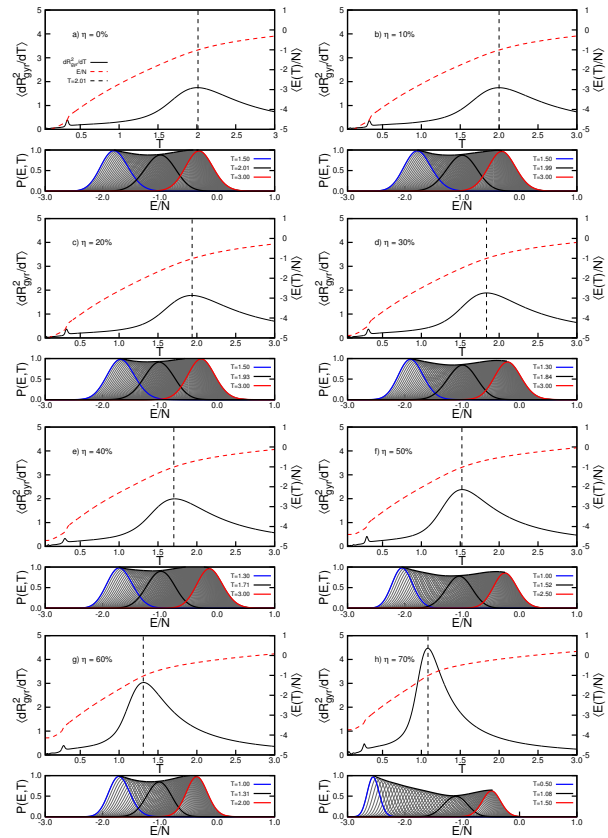


FIG. 6: (Color online) This figures show the analysis of the continuous structural transitions for  $\eta = 0, 10, \dots, 70\%$ .  $\langle dR_{\text{gyr}}^2(T) / dT \rangle$  is shown as a solid black line in the upper graphics and the energy  $\langle E(T) \rangle$  is shown as a dashed red curve. The vertical dashed black line marks the transition temperature. Below each figure for  $\langle dR_{\text{gyr}}^2(T) / dT \rangle$  is shown  $P(E, T = T)$ , in the vicinity of  $T = T^{\text{tr}}$ . The highlighted curves, solid blue, solid red are the distributions for liquid (globular) and coil phases, respectively. The black solid line shows the transition. The temperatures are given in the insets.

energy

$$\begin{aligned} \frac{\partial F^{\text{MAX}}(E, T)}{\partial E} &= -\frac{d^2 \ln g(E)}{dE^2} [E - F(T)] = 0 \\ &= -\gamma(E) [E - F(T)] = 0. \end{aligned} \quad (35)$$

The conditions at which the derivative is zero are *i*)  $\gamma(E) = 0$ , which does not lead to a maximum at the probability distribution, and *ii*)  $E - F(T) = 0$ , where  $E$  is the microcanonical energy. A derivative of equation 35, at the condition that maximizes the probability leads to

$$\frac{\partial^2 F^{\text{MAX}}(E, T)}{\partial E^2} = -\gamma(E). \quad (36)$$

So, for the initial assumption to hold (the peak distribution has a minimum value at  $T = T^{\text{tr}}$  in comparison with adjacent temperatures), its second derivative must

be positive,  $\gamma(E) < 0$ , which coincides with the microcanonical condition for the fugacity.

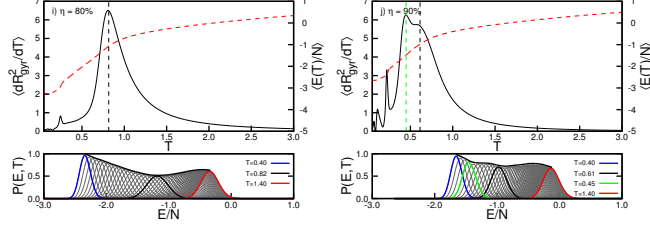


FIG. 7: (Color online) The same as in figure 6 for  $\eta = 80\%$  and  $90\%$ . The  $\eta = 80\%$  curve is essentially the same as for lower  $\eta$ , however, for  $\eta = 90\%$  the coil-globular transition splits up in two, represented by the green and black curves.

identify a wrapping curve with a very well defined minimum which gives the transition temperature. Out of the transition the system is continuously driven to the coil or globular phase. At high ligand concentration ( $\eta > 60\%$ ), the probability distributions become asymmetric. This asymmetry is related to the energy barrier of the  $V_{YK}$  potential that the polymer has to cross to undergo a transition. For lower concentrations the asymmetry does not exist. At all ligand concentrations and low temperature, it is possible to identify the first order transition as a change in the concavity of the energy and a small peak in  $\langle dR^2_{\text{gyr}}(T) / dT \rangle$ . At  $\eta = 100\%$  the first order peak is wiped out, instead, three second order transitions show up as seen in Fig. 8. Recent works have shown structural transitions for single chain polyampholytes in agreement with our findings [49, 50].

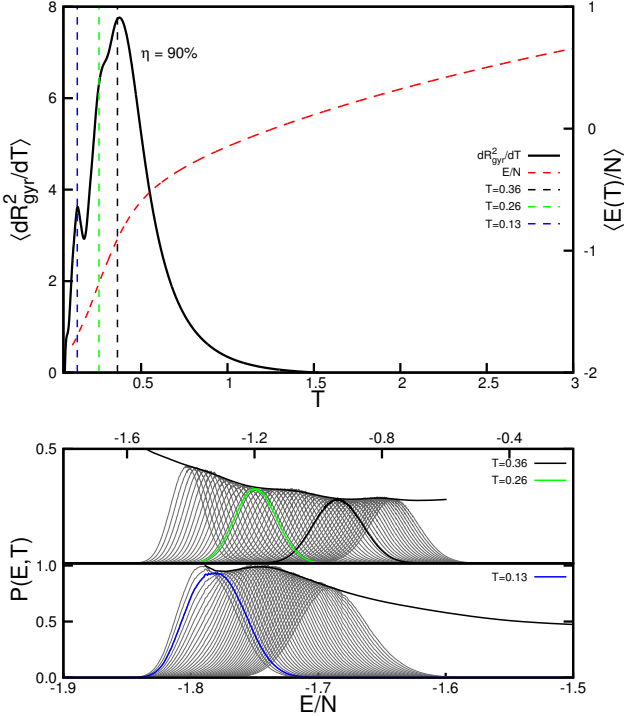


FIG. 8: (Color online) Energy and radius of gyration are shown in the figure at the top. In the bottom figures are the probability distribution. Two minima are seen in the first plot. The more detailed figure shows the existence of a minimum slightly above  $E/N \approx -1.8$ .

In Figs. 6 and 7 a quantitative analysis of the continuous structural transitions are shown. We present in those figures the radius of gyration (black solid line) and the energy (red dashed line) as a function of temperature. Below those quantities we show the corresponding probability distribution  $P(E, T)$  for various different temperatures. The highlighted curves are for  $T$  slightly below (blue curve) and above (red curve) the transition temperature  $T_c$ , which is shown in the bold black curve. Accumulating many of such curves in the same plot allow us to

#### D. Bond-bond correlations

Considering the more general Eq. 8 for the second moment segment size near the  $\Theta$ -point together with the corresponding bond-bond correlation in Eq. 9, we can set the scenario to understand the mechanical properties of a single chain polymer with quenched disorder at the hyperphase diagram near the CG structural transition line. We tackle this problem as follows. During the last iteration of the WL simulation, an equilibrium configuration is stored for each energy bin. After thermodynamic integration, the equilibrium energy at each  $(T, \eta)$  point of interest is calculated and the configuration is used to start a Metropolis simulation with Simulated Annealing. Sampling structural properties in a generalized ensemble simulation is not a trivial task. The number of MC steps required for a polymer configuration to become uncorrelated depends both on the quantity measured and the temperature. Recent studies showed that autocorrelation times of structural quantities diverge due to critical slowing down and are indeed an indicator of structural transitions [51]. The values of  $(T, \eta)$  points of the hyperphase diagram (depicted in Figure 4) are located at the extended phase, which means that only points near and above the CG transition line were sampled. The CG transition temperature for each chain length is calculated according to a scaling law predicted for  $\eta = 0\%$ . The values were calculated using a scaling law from Ref. [37] and are summarized in Table I. The chain lengths of  $N = 50, 70, 100, 200$  and  $1,000$  monomers were simulated from  $\eta = 0\%$  to  $\eta = 100\%$  with a  $10\%$  increment. For error analysis, 100 independent simulations were performed for each chain size at every  $(T, \eta)$  point.

TABLE I:  $T_{CG}$  for different chain sizes.

$N$ ( $\eta = 0\%$ )	$T_{CG}$
50	1.77(3)
70	2.00(1)
100	2.13(2)
200	2.38(7)
1,000	2.81(2)

We divided the hyperphase diagram in three regions of interest: *i*)  $T \gg T_{CG}$ , or the good solvent region, where the interactions are entropically-driven and EV contributes to a SAW regime; *ii*)  $T > T_{CG}$  where the enthalpically-driven interactions begin to compete with EV; and *iii*)  $T \approx T_{CG}$ , or the athermal solvent, where both enthalpic and entropic potentials are of the same order of magnitude, thus fulfilling the requirements of the Flory's hypothesis.

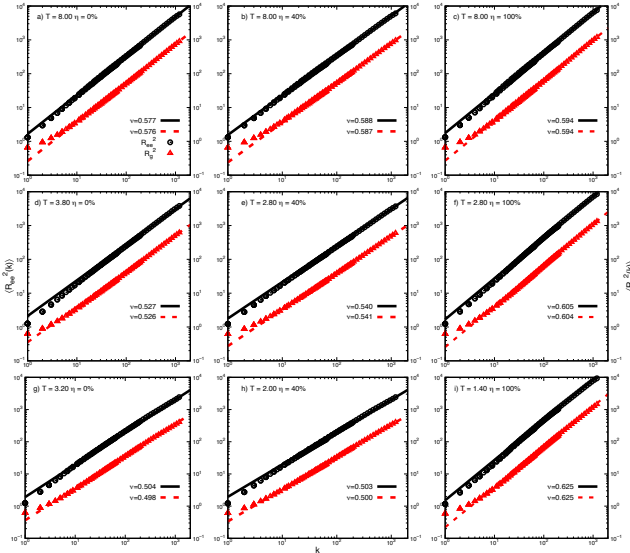


FIG. 9: (color online). Log-log plot of squared end-to-end distance  $\langle R_{ee}^2(k) \rangle$  (black circles and the scale at the left  $y$  axis) and radius of gyration  $\langle R_g^2(k) \rangle$  (red triangles and the scale at the left  $y$  axis) as a function of the distance  $k = |i - j|$ . The fitting lines are shown as black solid lines and red dashed line, respectively. From top to bottom:  $T = (a - c) 8.00$ , (d) 3.80, (e - f) 2.80, (g) 3.20, (h) 2.00 and (i) 1.40.  $\eta = 0\%$  is shown at the left panels,  $\eta = 40\%$  at the middle panels and  $\eta = 100\%$  at the right panel.

In Figures 9 to 12, the points are first summed and normalized over all  $k = |i - j|$  distances between monomers  $i$  and  $j$  along the chain, and then averaged over 100 independent simulations, where the standard deviations for each point are collected. As correlations tend to become noisy as  $k$  increases, the linear regression fitting is stabilized by the weights of the error values (not shown for clarity). The panels show concentrations  $\eta = 0\%$ , 40%, and 100% and three values of temperature are chosen for each concentration.

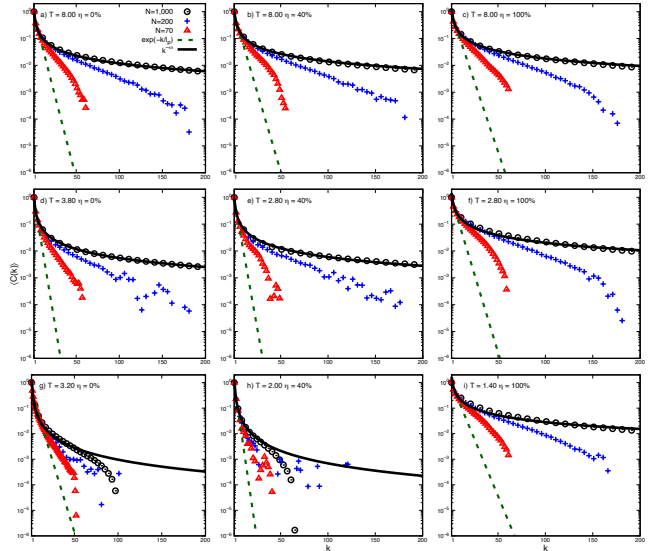


FIG. 10: (color online). Semi-log plot of the bond-bond correlations  $\langle C(k) \rangle$  as a function of the distance  $k = |i - j|$ . Symbols account for different chain sizes:  $N = 70$  (red triangles) 200 (blue crosses) and 1,000 (black circles). The exponential fit (Eq. 2) is the black solid line. For comparison, the power-law fit (Eq. 3) is shown as a green dashed line. From top to bottom:  $T = (a - c) 8.00$ , (d) 3.80, (e - f) 2.80, (g) 3.20, (h) 2.00 and (i) 1.40.  $\eta = 0\%$  is shown at the left panels,  $\eta = 40\%$  at the middle panels and  $\eta = 100\%$  at the right panel.

In Fig. 9 the squared segment chain sizes are plotted in a log-log scale as a function of  $k$ . Black circles are used for  $\langle R_{ee}^2(k) \rangle$  (plotted at the left  $y$  axis and adjusted with a black solid line), while red triangles represent the  $\langle R_g^2(k) \rangle$  (plotted at the right  $y$  axis and adjusted with a red dashed line) for all chain lengths. Both fitting exponents are shown at the bottom right side of each panel. Estimating accurate values for diluted polymers is challenging, as finite-size effects add up to leading corrections for small  $k$ . So, an arbitrary starting value for  $k$  is chosen and, as new segment points are included, the fitting is iteratively adjusted, following the recipe in Ref. [52], where we have also observed that  $\chi^2$  stabilizes for large  $k$ . At  $T = 8.00$  (panels *a* - *c*) the polymer is at the SAW phase: in *a*)  $\eta = 0\%$  and  $\nu = 0.572$ ; in *b*)  $\eta = 40\%$  and  $\nu = 0.588$ ; and in *c*)  $\eta = 100\%$  and the exponent  $\nu = 0.594$  is slightly higher than the SAW value, as the ligand-ligand repulsion leads to a swollen chain due to an excess in EV. It is worth noting that at the EV phase the leading correction does not contribute to the fitting whatsoever. As the temperature is lowered (panels *d* - *f*) we expect a decrease in  $\nu$  towards the Gaussian value, as the solvent-induced EV decreases. Also, a decrease in the segment chain size is accompanied by the proportional increase of the leading correction. Indeed in *d*)  $\nu = 0.527$  for  $T = 3.80$  and in *e*)  $\nu = 0.540$  for  $T = 2.80$ . However, in *f*) the exponent increases to  $\nu = 0.606$  when the temperature decreases to  $T = 2.80$ . In the final panels the temperature was set such that the chain is still ex-

tended and in the vicinity of  $\nu \approx 1/2$ . In *g*)  $T = 3.20$  with  $\nu = 0.501(3)$  while in panel *h*)  $T = 2.00$   $\nu = 0.501(1)$ . In panel *i*) the exponent increases to  $\nu = 0.620$  at the lowest temperature simulated of  $T = 1.40$ . This can be interpreted as a transition towards a more rigid phase, in agreement with the zig-zag structure previously observed.

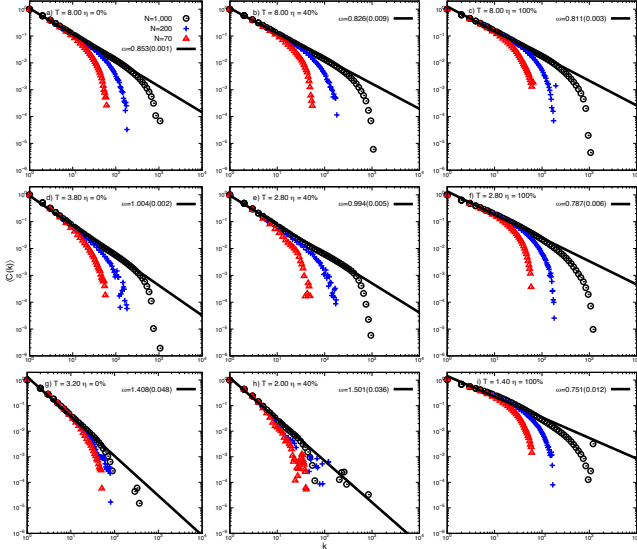


FIG. 11: (color online). Log-log plot of the bond-bond correlations  $\langle C(k) \rangle$  as a function of the distance  $k = |i - j|$ . Symbols account for different chain sizes:  $N = 70$  (red triangles) 200 (blue crosses) and 1,000 (black circles). The power-law fit (Eq. 3) is shown as a black solid line. From top to bottom:  $T = (a - c) 8.00$ ,  $(d - f) 3.80$ ,  $(e - f) 2.80$ ,  $(g) 3.20$ ,  $(h) 2.00$  and  $(i) 1.40$ .  $\eta = 0\%$  is shown at the left panels,  $\eta = 40\%$  at the middle panels and  $\eta = 100\%$  at the right panel. From top to bottom is shown  $T = 3.00$  (*a*),  $T = 2.50$  (*b*) and  $T = 2.00$  (*c*). Symbols account for different concentrations  $\eta = 0\%$  (open squares) 50% (open circles) and 100% (crosses), being the power-law fit represented respectively by the black solid, red dotted and blue dashed curves, respectively.

In Figs. 10, 11 and 12 we chose different symbols and colors for each chain length as finite-size effects are more pronounced. Red triangles for  $N = 70$ , blue crosses for  $N = 200$  and black circles for  $N = 1,000$ . The  $(T, \eta)$  values in each panel are the same as in Fig. 9. We first investigate the exponential decay hypothesis, predicted for Gaussian chains (Eq. 2).  $\langle C(k) \rangle$  is plotted in a semi-log scale. The dashed green line is the exponential fit of Eq. 2 for the first few monomers,  $1 < k \ll N$ , while the solid black curve is the power-law fit with Eq. 3 over  $1 \ll k \ll N$ . The data is better fit by the power-law decay, and becomes more clear for large  $N$ , where finite-size effects are diminished. So, it means that the exponential fitting of  $1/\ell_P$  from the first-neighbors is size-dependent and corrections must be applied [24]. In polymer chains where bending restraints are present, an exponential decay is observed for small  $k$ , however scaling arguments have proven that for long chains the power-law regime

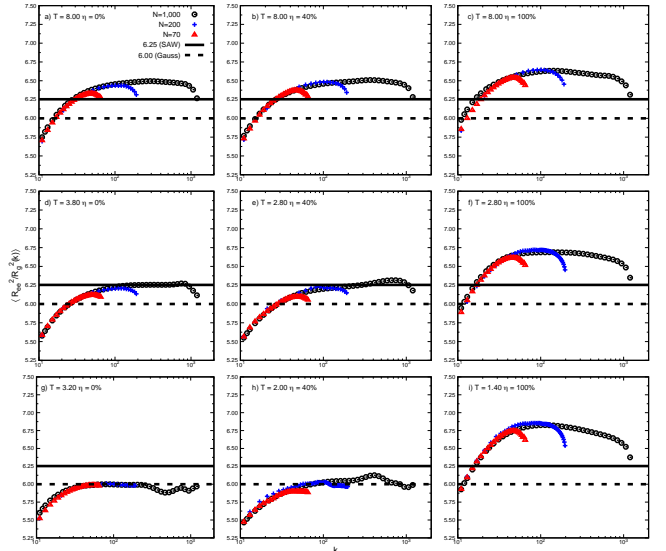


FIG. 12: (color online). Ratio between end-to-end and radius of gyration  $\langle R_{ee}^2 / R_g^2(k) \rangle$  as a function of the chain segment size  $k = |i - j|$ . Symbols account for different chain sizes:  $N = 70$  (red triangles) 200 (blue crosses) and 1,000 (black circles). The SAW value of 6.25 is shown as a black solid line, and the Gaussian value of 6.00 is shown as black dashed line. From top to bottom:  $T = (a - c) 8.00$ ,  $(d) 3.80$ ,  $(e - f) 2.80$ ,  $(g) 3.20$ ,  $(h) 2.00$  and  $(i) 1.40$ .  $\eta = 0\%$  is shown at the left panels,  $\eta = 40\%$  at the middle panels and  $\eta = 100\%$  at the right panel. From top to bottom is shown  $T = 3.00$  (*a*),  $T = 2.50$  (*b*) and  $T = 2.00$  (*c*). Symbols account for different concentrations  $\eta = 0\%$  (open squares) 50% (open circles) and 100% (crosses).

still dominates, and quantities can be rescaled by  $1/\ell_P$  [53]. To investigate the power-law hypothesis, the log-log plot of  $\langle C(k) \rangle$  is shown in Fig. 11. The  $(\eta, T)$  values are the same as in Fig. 10, as well as the symbols. The solid black line is the best fit of  $\omega$  for  $1 < k \ll 10^3$ .

At  $T = 8.00$  (panels *a* – *c*) the polymer is at the SAW phase: in *a*)  $\eta = 0\%$   $\omega = 0.853(1)$ ; in *b*)  $\eta = 40\%$   $\omega = 0.826(9)$ ; and in *c*)  $\eta = 100\%$  the exponent  $\omega = 0.811(3)$ . As observed in Fig. 9, these values are also in the vicinity of the SAW value. As the temperature is lowered (panels *d* – *f*) we expect an increase in  $\omega$  towards the Gaussian value. In *d*)  $\omega = 1.004(2)$  for  $T = 3.80$  and in *e*)  $\omega = 0.994(5)$  for  $T = 2.80$ . Again, in *f*) the exponent decreases (in agreement with the closure relation between  $\nu$  and  $\omega$ ) to  $\omega = 0.787(6)$  when the temperature decreases to  $T = 2.80$ . In *g*)  $T = 3.20$  with  $\omega = 1.408(48)$  while in panel *h*)  $T = 2.00$   $\omega = 1.501(36)$ . In panel *i*) the exponent decreases to  $\omega = 0.751(12)$  at the lowest temperature simulated of  $T = 1.40$ .

It has been shown [52] that the ratio  $\langle R_{ee}^2 / R_g^2(k) \rangle$  is also a universal quantity. The SAW limit leads to a ratio of 6.25, while the Gaussian regime leads to a ratio of 6. In Fig. 12 we can see that in the upper panels the ratio reaches the SAW limit from above, as the chain is in a swollen configuration. In contrast, at the panels *g* – *h*),

the Gaussian limit is reached from below, as the leading correction  $\propto k^{1/2}$  implies. It is also worth noting that for  $\eta = 100\%$  the swelling of the polymer chain increases when  $T$  is lowered, in agreement with our findings from both exponents  $\nu$  and  $\omega$ .

### E. Validation of the power law exponents

The clear power-law decay is a direct result of logarithmic corrections, and no indications of Gaussian behavior are found over three decades. At concentrations  $\eta = 100\%$  the exponent remains near the SAW limit for all temperatures. Below this concentration, a transition towards the gaussian limit occurs, and for  $\eta = 40\%$  the predicted exponent  $\omega = 1.50$  dominates. The closure relationship  $\omega = 2(1 - \nu)$  for the SAW phase is met, while near the expected Gaussian regime, we observe that  $\omega = d\nu$  being  $d$  the dimensionality of the system. The finiteness of the polymer chains leads to intermediate values of  $\omega$ , which are difficult to interpret as the system is neither in the pure EV nor at the Gaussian condition. Once the chain segment size obeys a power-law, and the leading corrections dominate near the Gaussian regime (as the chain segment ratio reaches the Gaussian value from below) the bond-bond correlations decay as a power law in any conditions. Previous simulations with diluted polyelectrolytes have found a scaling exponent  $\nu$  that, upon counterion concentration changes, undergoes a variation that is consistent with the crossover between the Gaussian and SAW regimes [54]. More recent results placed the scaling exponent  $\nu \approx 0.824$  for polyelectrolytes at similar conditions [55], in agreement with the SAW model. Recent experiments also shown that both coil and globule domains may exist within a single confined DNA chain [56].

## V. CONCLUSIONS

In summary, we have observed that polymer thermodynamics is directly affected by the introduction of lig-

ands, as expected by the pairwise quenched disorder [57]. The hyperphase diagram for  $N = 70$  monomers is accurately reported shown in Fig. 4 (a), showing a monotonic lowering of  $T_{CG}$  when  $\eta$  increases. Our model matches previous results of  $T_{CG}$  for  $\eta = 0\%$  [37]. The system has three identified phases. A disordered phase,  $(C, C^*)$ , at  $T > T_{CG}$ , a liquid globular,  $(G, G^*)$ , at  $T_{SG} < T < T_{CG}$  and a solid phase at  $T < T_{SG}$ , with both solid globular,  $(S)$ , and helical,  $(H)$ , structures. Those phases are shown in Fig. 4 (b). When the ligand concentration is high, EV repulsion is strong, and a liquid globular structure is not stable anymore. Competition between EV and LJ attraction leads to a zig-zag configuration, which is stable. Bond-bond correlations are reported for long chains  $N$  up to  $10^3$  monomers, where  $T_{CG}$  is predicted by a scaling law. At all temperatures investigated, no exponential decay is observed. For  $\eta = 100\%$ , the power law exponent is consistent with a SAW limit. At intermediate to zero  $\eta$  and  $T \approx T_{CG}$ , a crossover is observed and  $\omega = 1.50$  is a signature of remaining logarithmic corrections. A suggestion for future experiments would be to adjust the force *versus* extension data with models that directly account for EV interactions and power-law decay in bond-bond correlations, like in ssDNA or small DNA sequences. Still interesting is to simulate the same system in a steady state situation, allowing the monomers to move from site to site or from the polymer chain to the solvent and vice-versa. However, this case can be problematic since the thermodynamic of annealed statistics may introduce systematic changes on the structural transitions, making the scaling analysis more challenging.

## VI. ACKNOWLEDGMENTS

The authors gratefully acknowledge financial support from CNPq and FAPEMIG (Brazilian Agencies) under Grants CNPq 402091/2012-4 and FAPEMIG RED-00458-16.

---

[1] E. Kay, D. Leigh, and F. Zerbetto, *Angewandte Chemie International Edition* **46**, 72 (2007), ISSN 1521-3773, URL <http://dx.doi.org/10.1002/anie.200504313>.

[2] I. D. Kuntz, *Science* **257**, 1078 (1992), ISSN 0036-8075, URL <http://science.scienmag.org/content/257/5073/1078.full.pdf>.

[3] D. Hu, J. Yu, K. Wong, B. Bagchi, P. J. Rossky, and P. F. Barbara, *Nature* **405**, 1030 (2000), URL <http://dx.doi.org/10.1038/35016520>.

[4] V. A. Bloomfield, *Current Opinion in Structural Biology* **6**, 334 (1996), ISSN 0959-440X, URL <http://www.sciencedirect.com/science/article/pii/S0959440X96800522>.

[5] K. G. Strothkamp and S. J. Lippard, *Proceedings of the National Academy of Sciences* **73**, 2536 (1976), <http://www.pnas.org/content/73/8/2536.full.pdf>, URL <http://www.pnas.org/content/73/8/2536.abstract>.

[6] S. M. Cohen and S. J. Lippard, *Progress in nucleic acid research and molecular biology* **67**, 93 (2001).

[7] J. B. Chaires, N. Dattagupta, and D. M. Crothers, *Biochemistry* **21**, 3933 (1982), pMID: 7126524, URL <http://dx.doi.org/10.1021/bi00260a005>.

[8] J. van Noort, S. Verbrugge, N. Goosen, C. Dekker, and R. T. Dame, *Proceedings of the National Academy of Sciences* **100**, 12522 (2003), URL <http://dx.doi.org/10.1073/pnas.1231002100>.

of Sciences of the United States of America **101**, 6969 (2004), URL <http://www.ncbi.nlm.nih.gov/pmc/articles/PMC406450/>.

[9] M. S. Rocha, M. C. Ferreira, and O. N. Mesquita, The Journal of Chemical Physics **127**, 105108 (2007), URL <http://scitation.aip.org/content/aip/journal/jcp/127/10/10.1063/1.2768945>.

[10] B. H. Geierstanger and D. E. Wemmer, Annual review of biophysics and biomolecular structure **24**, 463 (1995).

[11] P. L. Hamilton and D. P. Arya, Nat. Prod. Rep. **29**, 134 (2012), URL <http://dx.doi.org/10.1039/C1NP00054C>.

[12] E. Allahyarov, H. Löwen, and L. Zhu, Phys. Chem. Chem. Phys. **18**, 19103 (2016), URL <http://dx.doi.org/10.1039/C6CP03149H>.

[13] P.-G. d. Gennes, scaling concepts in polymer physics (Cornell University Press, 1979).

[14] M. Rubinstein and R. H. Colby, *Polymer Physics* (Oxford University Press, 2003).

[15] S. B. Smith, L. Finzi, and C. Bustamante, Science **258**, 1122 (1992).

[16] J. F. Marko and E. D. Siggia, Macromolecules **28**, 8759 (1995), <http://dx.doi.org/10.1021/ma00130a008>, URL <http://dx.doi.org/10.1021/ma00130a008>.

[17] L. Siman, I. S. S. Carrasco, J. K. L. da Silva, M. C. de Oliveira, M. S. Rocha, and O. N. Mesquita, Phys. Rev. Lett. **109**, 248103 (2012), URL <http://link.aps.org/doi/10.1103/PhysRevLett.109.248103>.

[18] L. Schäfer, *Excluded volume effects in polymer solutions: as explained by the renormalization group* (Springer Science & Business Media, 2012).

[19] P. J. Flory, The Journal of Chemical Physics **17**, 303 (1949), URL <http://scitation.aip.org/content/aip/journal/jcp/17/3/10.1063/1.1747243>.

[20] J. P. Wittmer, H. Meyer, J. Baschnagel, A. Johner, S. Obukhov, L. Mattioni, M. Müller, and A. N. Semenov, Phys. Rev. Lett. **93**, 147801 (2004), URL <http://link.aps.org/doi/10.1103/PhysRevLett.93.147801>.

[21] J. P. Wittmer, P. Beckrich, H. Meyer, A. Cavallo, A. Johner, and J. Baschnagel, Phys. Rev. E **76**, 011803 (2007), URL <http://link.aps.org/doi/10.1103/PhysRevE.76.011803>.

[22] J. P. Wittmer, A. Cavallo, H. Xu, J. E. Zabel, P. Polińska, N. Schulmann, H. Meyer, J. Farago, A. Johner, S. P. Obukhov, et al., Journal of Statistical Physics **145**, 1017 (2011), URL <https://doi.org/10.1007/s10955-011-0354-0>.

[23] D. Shirvanyants, S. Panyukov, Q. Liao, and M. Rubinstein, Macromolecules **41**, 1475 (2008), <http://dx.doi.org/10.1021/ma071443r>, URL <http://dx.doi.org/10.1021/ma071443r>.

[24] H.-P. Hsu, W. Paul, and K. Binder, Polymer Science Series C **55**, 39 (2013), ISSN 1555-614X, URL <http://dx.doi.org/10.1134/S1811238213060027>.

[25] M.-N. Dessinges, B. Maier, Y. Zhang, M. Peliti, D. Bensimon, and V. Croquette, Phys. Rev. Lett. **89**, 248102 (2002), URL <http://link.aps.org/doi/10.1103/PhysRevLett.89.248102>.

[26] N. M. Toan and D. Thirumalai, The Journal of Chemical Physics **136**, 235103 (2012), URL <http://scitation.aip.org/content/aip/journal/jcp/136/23/10.1063/1.4729371>.

[27] M. J. Stevens, D. B. McIntosh, and O. A. Saleh, Macromolecules **46**, 6369 (2013), <http://dx.doi.org/10.1021/ma401211w>, URL <http://dx.doi.org/10.1021/ma401211w>.

[28] F. Wang and D. P. Landau, Phys. Rev. Lett. **86**, 2050 (2001), URL <http://link.aps.org/doi/10.1103/PhysRevLett.86.2050>.

[29] D. T. Seaton, S. Schnabel, D. P. Landau, and M. Bachmann, Phys. Rev. Lett. **110**, 028103 (2013), URL <http://link.aps.org/doi/10.1103/PhysRevLett.110.028103>.

[30] M. J. Williams and M. Bachmann, Phys. Rev. Lett. **115**, 048301 (2015), URL <http://link.aps.org/doi/10.1103/PhysRevLett.115.048301>.

[31] T. X. Hoang, H. L. Trinh, A. Giacometti, R. Podgornik, J. R. Banavar, and A. Maritan, Phys. Rev. E **92**, 060701 (2015), URL <http://link.aps.org/doi/10.1103/PhysRevE.92.060701>.

[32] K. Lewandowski and M. Banaszak, Phys. Rev. E **84**, 011806 (2011), URL <http://link.aps.org/doi/10.1103/PhysRevE.84.011806>.

[33] T. Vogel, Y. W. Li, T. Wüst, and D. P. Landau, Phys. Rev. Lett. **110**, 210603 (2013), URL <https://link.aps.org/doi/10.1103/PhysRevLett.110.210603>.

[34] S. Schnabel, M. Bachmann, and W. Janke, The Journal of Chemical Physics **131**, 124904 (2009), URL <http://scitation.aip.org/content/aip/journal/jcp/131/12/10.1063/1.3223720>.

[35] G. Grinstein and A. Luther, Physical Review B **13**, 1329 (1976).

[36] S. Kirkpatrick, M. P. Vecchi, et al., science **220**, 671 (1983).

[37] D. T. Seaton, T. Wüst, and D. P. Landau, Phys. Rev. E **81**, 011802 (2010), URL <http://link.aps.org/doi/10.1103/PhysRevE.81.011802>.

[38] F. Rampf, W. Paul, and K. Binder, EPL (Europhysics Letters) **70**, 628 (2005), URL <http://stacks.iop.org/0295-5075/70/i=5/a=628>.

[39] J. C. S. Rocha, S. Schnabel, D. P. Landau, and M. Bachmann, Phys. Rev. E **90**, 022601 (2014), URL <http://link.aps.org/doi/10.1103/PhysRevE.90.022601>.

[40] S. Schnabel, W. Janke, and M. Bachmann, Journal of Computational Physics **230**, 4454 (2011).

[41] J. Gross, T. Neuhaus, T. Vogel, and M. Bachmann, The Journal of chemical physics **138**, 074905 (2013).

[42] P. Chi, B. Li, and A.-C. Shi, Phys. Rev. E **84**, 021804 (2011), URL <http://link.aps.org/doi/10.1103/PhysRevE.84.021804>.

[43] K. A. Dill and D. Shortle, Annual Review of Biochemistry **60**, 795 (1991), pMID: 1883209, <http://dx.doi.org/10.1146/annurev.bi.60.070191.004051>, URL <http://dx.doi.org/10.1146/annurev.bi.60.070191.004051>.

[44] M. E. Fisher, Reviews of Modern Physics **70**, 653 (1998).

[45] B. V. d. Costa, L. A. d. S. Mól, and J. C. S. Rocha, Computer Physics Communications **216**, 77 (2017).

[46] K. e. a. Binder, International Journal of Modern Physics C **106**, 659 (2014).

[47] K. e. a. Binder, International Journal of Modern Physics C **106**, 659 (2014).

[48] K. e. a. Binder, International Journal of Modern Physics C **106**, 659 (2014).

[49] V. Yamakov, A. Milchev, H. Jörg Limbach, B. Dünweg, and R. Everaers, Phys. Rev. Lett. **85**, 4305 (2000), URL <https://link.aps.org/doi/10.1103/PhysRevLett.85.4305>.

[50] R. G. Winkler, M. O. Steinhauser, and P. Reineker, Phys. Rev. E **66**, 021802 (2002), URL <https://link.aps.org/doi/10.1103/PhysRevE.66.021802>.

doi/10.1103/PhysRevE.66.021802.

[51] K. Qi and M. Bachmann, The Journal of Chemical Physics **141**, 074101 (2014), ISSN 1089-7690, URL <http://dx.doi.org/10.1063/1.4891800>.

[52] N. Clisby, Phys. Rev. Lett. **104**, 055702 (2010), URL <https://link.aps.org/doi/10.1103/PhysRevLett.104.055702>.

[53] A. Huang, A. Bhattacharya, and K. Binder, The Journal of Chemical Physics **140**, 214902 (2014), URL <http://scitation.aip.org/content/aip/journal/jcp/140/21/10.1063/1.4879537>.

[54] P.-Y. Hsiao and E. Luijten, Physical review letters **97**, 148301 (2006).

[55] F. Alarcón, G. Pérez-Hernández, E. Pérez, and A. G. Goicochea, European Biophysics Journal **42**, 661 (2013).

[56] B. Sung, A. Leforestier, and F. Livolant, Nucleic Acids Research (2015), URL <http://nar.oxfordjournals.org/content/early/2015/12/22/nar.gkv1494.abstract>.

[57] K. Binder and W. Kob, Glassy materials and disordered solids: An introduction to their statistics (World Scientific, 2011).

[58] D. B. McIntosh, G. Duggan, Q. Gouil, and O. A. Saleh, Biophysical journal **106**, 659 (2014).